Draft version December 5, 2019
Typeset using LaTeX **twocolumn** style in AASTeX62

Implications of the search for optical counterparts during the first six months of the Advanced LIGO's and Advanced Virgo's third observing run: possible limits on the ejecta mass and binary properties

Michael W. Coughlin,[1] Tim Dietrich,[2] Sarah Antier,[3] Mattia Bulla,[4,5] Francois Foucart,[6] Kenta Hotokezaka,[7] Geert Raaijmakers,[8] Tanja Hinderer,[8] and Samaya Nissanke[8,9]

[1] *California Institute of Technology, 1200 East California Blvd, MC 249-17, Pasadena, CA 91125, USA*
[2] *Nikhef, Science Park, 1098 XG Amsterdam, The Netherlands*
[3] *APC, UMR 7164, 10 rue Alice Domon et Lonie Duquet, 75205 Paris, France*
[4] *Nordita, KTH Royal Institute of Technology and Stockholm University, Roslagstullsbacken 23, SE-106 91 Stockholm, Sweden*
[5] *Oskar Klein Centre, Department of Physics, Stockholm University, SE-106 91 Stockholm, Sweden*
[6] *Department of Physics & Astronomy, University of New Hampshire, 9 Library Way, Durham NH 03824, USA*
[7] *Department of Astrophysical Sciences, Princeton University, Princeton, NJ 08544, USA*
[8] *GRAPPA, Anton Pannekoek Institute for Astronomy and Institute of High-Energy Physics, University of Amsterdam, Science Park 904, 1098 XH Amsterdam, The Netherlands*
[9] *Nikhef, Science Park 105, 1098 XG Amsterdam, The Netherlands*

ABSTRACT

GW170817 showed that neutron star mergers not only emit gravitational waves but also can release electromagnetic signatures in multiple wavelengths. Within the first half of the third observing run of the Advanced LIGO and Virgo detectors, there have been a number of gravitational wave candidates of compact binary systems for which at least one component is potentially a neutron star. In this article, we look at the candidates S190425z, S190426c, S190510g, S190901ap, and S190910h, predicted to have potentially a non-zero remnant mass, in more detail. All these triggers have been followed up with extensive campaigns by the astronomical community doing electromagnetic searches for their optical counterparts; however, according to the released classification, there is a high probability that some of these events might not be of extraterrestrial origin. Assuming that the triggers are caused by a compact binary coalescence and that the individual source locations have been covered during the EM follow-up campaigns, we employ three different kilonova models and apply them to derive possible constraints on the matter ejection consistent with the publicly available gravitational-wave trigger information and the lack of a kilonova detection. These upper bounds on the ejecta mass can be related to limits on the maximum mass of the binary neutron star candidate S190425z and to constraints on the mass-ratio, spin, and NS compactness for the potential black hole-neutron star candidate S190426c. Our results show that deeper electromagnetic observations for future gravitational wave events near the horizon limit of the advanced detectors are essential.

Keywords: gravitational waves, methods: statistical

1. INTRODUCTION

By the combined detection of GW170817, AT2017gfo, and GRB170817A, the field of multi-messenger astronomy was ushered into a new era in which gravitational-wave (GW) and electromagnetic (EM) signatures are simultaneously measured and analyzed, e.g., Abbott B. P. (2017); Abbott et al. (2017b); Arcavi et al. (2017); Coulter et al. (2017); Lipunov et al. (2017); Mooley et al. (2017); Savchenko et al. (2017); Soares-Santos et al. (2017); Tanvir et al. (2013); Troja et al. (2017); Valenti et al. (2017). Joint analyses allow a better understanding of the supranuclear-dense matter inside neutron stars (NSs) (e.g. Radice et al. (2018); Radice & Dai (2019); Bauswein et al. (2017); Margalit & Metzger (2017); Rezzolla et al. (2018); Coughlin et al. (2018b,a); Capano et al. (2019)), a precise measurement of the speed of gravitational waves (Abbott et al. 2017c), an independent measurement of the expansion rate of the Universe (Abbott et al. 2017a; Hotokezaka et al. 2019; Coughlin et al. 2019a; Dhawan et al. 2019), and constraints on alternative models of gravity (Ezquiaga & Zumalacrregui 2017; Baker et al. 2017; Creminelli & Vernizzi 2017; Sakstein & Jain 2017).

In general, the merger of two compact objects from which at least one is a NS, is connected to a variety of possible EM signatures in almost all wavelengths. A

highly relativistic jet can produce a short gamma-ray burst (sGRB) lasting a few seconds (Eichler et al. 1989; Paczynski 1991; Narayan et al. 1992; Mochkovitch et al. 1993; Lee & Ramirez-Ruiz 2007; Nakar 2007) and a synchrotron afterglow in the X-rays, optical and radio visible bands for hours to months after the initial emission due to the deceleration of the jet into the ambient media (Sari et al. 1998). The ejection of highly neutron rich material, being the seed of r-process elements (Lattimer & Schramm 1974, 1976), powers a thermal ultraviolet/optical/near-infrared kilonova due to the radioactive decay of the new heavy elements produced in the ejecta (Li & Paczynski 1998; Metzger et al. 2010; Roberts et al. 2011; Kasen et al. 2017). Although the color and luminosity of a kilonova will be viewing angle dependent, the kilonova signature is, in contrast to the sGRB and its afterglow, likely visible from all viewing angles. This means that after every merger which ejects a sufficient amount of material, one should be able to observe a kilonova regardless of the orientation of the system (Roberts et al. 2011). Thus, kilonovae provide a *smoking guns* evidence for binary neutron star (BNS) and black hole - neutron star (BHNS) mergers.

However, current numerical relativity studies indicate that not all BNS or BHNS collisions will eject enough material to create EM signals as bright as the one observed for GW170817. For most BNS systems, the EM signals are expected to be dimmer than for GW170817 if a black hole (BH) forms directly after the moment of merger, since for these *prompt collapse* configurations the amount of ejected material and the mass of the potential debris disk is expected to be very small. Whether a merger remnant undergoes a prompt collapse depends mostly on its total mass (Bauswein et al. 2013; Hotokezaka et al. 2013; Dietrich & Ujevic 2017; Köppel et al. 2019; Agathos et al. 2019) but also seems to be sub-dominantly affected by the mass-ratio (Kiuchi et al. 2019). For highly asymmetric mass ratios ($m_1/m_2 \lesssim 0.8$), there could be a non-negligible ejecta mass and/or a massive accretion disk around the black hole remnant even for prompt collapse scenarios (Kiuchi et al. 2019).

In the case of a BHNS system, the brightness of the potential EM counterpart depends on whether the NS gets tidally disrupted by the BH and, thus, ejects a large amount of material and forms a massive accretion disk; or if the star falls into the BH without disruption, preventing the production of GRBs and kilonovae. Thus, the outcome of the merger is mostly determined by the mass ratio of the binary, the spin of the black hole, and the compactness of the NS, with disruption being favored for low-mass, rapidly rotating BH and large NS radii (Etienne et al. 2009; Pannarale et al. 2011; Foucart 2012; Kyutoku et al. 2015; Kawaguchi et al. 2016; Foucart et al. 2018).

Since the beginning of the third observation run, a number of potential GW events have triggered extensive follow-up campaigns to search for possible EM counterparts, most notably S190425z (LIGO Scientific Collaboration & Virgo Collaboration 2019a,b), S190426c (LIGO Scientific Collaboration & Virgo Collaboration 2019c,s), S190510g (LIGO Scientific Collaboration & Virgo Collaboration 2019f), S190814bv (LIGO Scientific Collaboration & Virgo Collaboration 2019o), S190901ap (LIGO Scientific Collaboration & Virgo Collaboration 2019t), S190910h (LIGO Scientific Collaboration & Virgo Collaboration 2019w), S190910d (LIGO Scientific Collaboration & Virgo Collaboration 2019v), S190923y (LIGO Scientific Collaboration & Virgo Collaboration 2019z), and S190930t (LIGO-Virgo collaboration 2019); cf. Tab. 1 for more details.[1] The large size of localization regions with thousands of square degrees have proved much more challenging to cover over short times than the ~ 20 square degrees of GW170817. In fact, no joint detection of GW and EM signals have been confirmed; see also Dado & Dar (2019) for a possible explanation that no sGRBs has been observed for the GW events within O3a. While a detection of an EM signature will help significantly to unravel some of the remaining open questions related to compact binary mergers, the possibility of a "missing" EM signature for an astrophysical relevant trigger whose sky location was covered during an EM follow-up campaign also delivers some information about the source properties, as we will discuss.

[1] Additional alerts have been sent out for other triggers, but those have been retracted. A BNS candidate S190718y (LIGO Scientific Collaboration & Virgo Collaboration 2019k) was sent to the astronomical community; due to the presence of a strong glitch near to the trigger time, only a few optical observations were performed and this alert will not be considered in this study. In addition, other candidates S190518bb (LIGO Scientific Collaboration & Virgo Collaboration 2019i), S190524q (LIGO Scientific Collaboration & Virgo Collaboration 2019j), S190808ae (LIGO Scientific Collaboration & Virgo Collaboration 2019n), S190816i (LIGO Scientific Collaboration & Virgo Collaboration 2019q) and S190822c (LIGO Scientific Collaboration & Virgo Collaboration 2019r) were also identified and later retracted. In addition, an interesting black hole merger candidate triggered intensive follow-up due to its low latency properties results with the possibility to have one object between 3 and 5 solar mass (LIGO Scientific Collaboration & Virgo Collaboration 2019l), but updated results with the full exploration of the parameter space of masses and spins, finally did not confirm these properties (LIGO Scientific Collaboration & Virgo Collaboration 2019m).

Table 1. Overview about officially non-retracted GW triggers with large probabilities to be BNS or BHNS systems. The individual columns refer to: the name of the event, an estimate using the most up-to-date classification for the event to be a BNS [p(BNS)], a BHNS [p(BHNS)], or terrestrial noise [p(terrestrial)] (Kapadia et al. 2019), and an indicator to estimate the probability of producing EM signature considering the candidate with astrophysical origin [p(HasRemnant)], whose definition is in the LIGO-Virgo alert userguide. Note that the alert can be also classified as "MassGap," completing the possible classifications. Note that within our analysis, we do not consider S190718y because of its very low probability to be of astrophysical origin.

Name	p(BNS)	p(BHNS)	p(terr.)	p(HasRemn.)
S190425z	$> 99\%$	0%	$< 1\%$	$> 99\%$
S190426c	24%	6%	58%	$> 99\%$
S190510g	42%	0%	58%	$> 99\%$
S190718y*	2%	0%	98%	$> 99\%$
S190814bv	0%	$> 99\%$	$< 1\%$	$< 1\%$
S190901ap	86%	0%	14%	$> 99\%$
S190910d	0%	98%	2%	$< 1\%$
S190910h	61%	0%	39%	$> 99\%$
S190923y	0%	68%	32%	$< 1\%$
S190930t	0%	74%	26%	$< 1\%$

In this article, we try to understand if from the detection or, more likely, non-detection of an EM counterpart to a potential GW event it is possible to place constraints on the merger outcome and the properties of the system. For this purpose, we will shortly summarize the EM follow-up campaigns of S190425z, S190426c, S190510g, S190814bv, S190901ap, S190910d, S190910h, S190923y, and S190930t in Sec. 2. We further also refer to Andreoni et al. (2019a) for a dedicated discussion done by the GROWTH collaboration about S190814bv.

In Sec. 3 we focus on the events for which the `HasRemnant`[2] prediction provides a high probability of a potential EM signature (S190425z, S190426c, S190510g, S190901ap, and S190910h)[3]; cf. Tab. 1. Under the assumption that the GW candidate location was covered during the EM observations, we will use a set of three different lightcurve models (Kasen et al. 2017; Bulla 2019; Hotokezaka & Nakar 2019) to predict the properties of the kilonova consistent with the non-observation of an EM counterpart. This analysis allows us to derive constraints on the maximum ejecta mass for each event in Sec. 3 and connects our findings to the binary properties in Sec. 4. These constraints are typically not very striking given the large distance to the GW triggers in the first half of advanced LIGO and advanced Virgo's third observing run, which highlights that, if possible, longer exposure times should be employed to reduce the possibility that interesting transients might be missed. We summarize our conclusions and lessons learned for observations in the second half of the third observing run in Sec. 5.

[2] https://emfollow.docs.ligo.org/userguide/content.html and https://dcc.ligo.org/LIGO-P1900291; Typically, the `HasRemnant` classification employs the disk mass estimate of Foucart et al. (2018) and applies to BHNS systems. BNS configurations are assumed to cause an EM signature, which, as we show later, might not be correct. The `HasRemnant` classification assumes the event to be of astrophysical origin and does not incorporate the possibility that the trigger is caused by noise

[3] We do not include S190718y because of its high probability to be noise.

2. EM FOLLOW-UP CAMPAIGNS

We summarize the EM follow-up work of the various teams that performed synoptic coverage of the sky localization area and who have circulated their findings in publicly available circulars during the first six months of the third observing run. For a summary of the follow-up campaign during the second observing run, please see Abbott B.P. (2019) and references therein. We differentiate the candidates by their classification (predominantly BNS in Table 2 and predominantly BHNS in Table 3). While this is mostly an initial classification and may change based on future offline estimates, we think it is useful as, for example, the distance estimates tend to be different between these classes. A short discussion about each candidate is presented below; note that we do not report the observations that exclusively target galaxies.

2.1. *S190425z*

LIGO/Virgo S190425z was identified by the LIGO Livingston Observatory (L1) and the Virgo Observatory (V1) at 2019-04-25 08:18:05.017 UTC (LIGO Scientific Collaboration & Virgo Collaboration 2019a,b). LIGO Hanford Observatory (H1) was not taking data at the time. It has been so far categorized as a BNS signal, reported as a BNS (99%) with a small probability of being in the mass gap ($< 1\%$). Due to the low signal-to-noise ratio (SNR) in V1, S190425z's sky localization is relatively poor, covering nearly $10,000$ square degrees. The original distance quoted for this system is 155 ± 45 Mpc, thus, about ~ 4 times further away than GW170817.

As the first alert during the O3 campaign with a high probability of having a counterpart, there was an intense follow-up campaign within the first ~ 72 hours after the initial notice (see ≈ 120 reports in GCN archive, mostly focusing on optical follow-up). As expressed in Cook et al. (2019), with more than 50,000 galaxies compatible with the 90% sky area volume due to the large

uncertainty of the localization, it was difficult to fully cover S190425z's localization. However, as shown in Table 2, ten telescopes reported tiling observations of the localization. For example, both the Zwicky Transient Facility (ZTF) (Bellm et al. 2018; Graham et al. 2019; Dekany et al. 2019; Masci et al. 2018), a camera and associated observing system on the Palomar 48 inch telescope, and Palomar Gattini-IR, a new wide-field near-infrared survey telescope at Palomar observatory, followed up S190425c extensively (Coughlin et al. 2019b). Covering about 8000 and 2200 square degrees respectively, the systems achieved depths of ≈ 21 $m_{\rm AB}$ in g- and r-bands with ZTF and 15.5 mag in J-band with Gattini-IR. Among them, using the LALInference skymap, about 21% of and 19% of the sky localization was covered by ZTF and Palomar Gattini-IR respectively. In addition, Pan-STARRS covered 28% of the bayestar sky localization area in g-band with a limiting magnitude of $i = 21.5$ mag (Smith et al. 2019); similarly, GOTO covered 30% of the initial skymap down to $L = 20.5$ mag (Steeghs et al. 2019a).

2.2. *S190426c*

LIGO/Virgo S190426c was identified by H1, L1, and V1 at 2019-04-26 15:21:55.337 UTC (LIGO Scientific Collaboration & Virgo Collaboration 2019c,s). With a probability of 58% to be terrestrial, S190426c might not be of astrophysical origin. But assuming that the signal is of astrophysical relevance, S190426c seems to be a BHNS system with relative probabilities of approximately 12 : 5 : 3 : 0 for the categories NSBH : MassGap : BNS : BBH, respectively (LIGO Scientific Collaboration & Virgo Collaboration 2019e). Within this analysis the `HasRemnant` probability is stated as 72%, thus, for all events with large `HasRemnant` predictions, is our best example for a possible BHNS merger. S190426c's sky localization, given that it was discovered by multiple interferometers, covers less area than S190425z. The initial 90% credible region was 1260 deg^2 with a luminosity distance of 375 ± 108 Mpc (LIGO Scientific Collaboration & Virgo Collaboration 2019c). The updated skymap, sent 48 hrs after the initial skymap, had a 90% credible region of 1130 deg^2 and a luminosity distance estimate of 377 ± 100 Mpc (LIGO Scientific Collaboration & Virgo Collaboration 2019d). As the first event announced with a significant probability of a BHNS nature, the interest in this event was large and about 70 circulars have been sent out (see the GCN archive). As shown in Table 3, 13 telescopes scanned the localization region; for example, ASAS-SN (Shappee et al. 2019), GOTO (Steeghs et al. 2019b), and ZTF (Kasliwal et al. 2019b) covered more than 50% of the sky localization area using multiple filters in the first 48 hrs.

2.3. *S190510g*

LIGO/Virgo S190510g was identified by H1, L1 and V1 at 2019-05-10 02:59:39.292 UTC (LIGO Scientific Collaboration & Virgo Collaboration 2019f). S190510g's latest sky localization covers 1166 deg^2 with a luminosity distance of 227 ± 92 Mpc (LIGO Scientific Collaboration & Virgo Collaboration 2019g). In the most recent update provided by the LIGO and Virgo Collaboration, the event is now more likely caused by noise (LIGO Scientific Collaboration & Virgo Collaboration 2019h) than it is to be an astrophysical source, with a probability of terrestrial (58%) and BNS (42%); however, since the event is, up to now, not officially retracted, we will consider it in this article. Due to its potential BNS nature and its trigger time being close to the beginning of the night in the Americas, the event was followed-up rapidly, with about 60 circulars produced (see GCN archive). With $\sim 65\%$ coverage of the LALInference skymap, GROWTH-DECam realized the deepest follow-up (Andreoni et al. 2019b). We can compute the joint coverage of different telescopes based upon their pointings and field of view reporting in the GCNs. Within 24 hr, CNEST, HMT, MASTER, Xinglong and TAROT, all with clear filters down to 18 mag, observed 71% of the LALInference sky localization area; this number would assuredly be higher with a coordinated effort.

2.4. *S190814bv*

The candidate S190814bv was identified by H1, L1, and V1 on 2019-08-14 21:10:39.013 UTC. First classified as a compact merger with one component having an initial mass between 3 and 5 solar masses (LIGO Scientific Collaboration & Virgo Collaboration 2019o), the candidate is now classified as a BHNS with posterior support from parameter estimation (Veitch et al. 2015) with NSBH (>99%) (LIGO Scientific Collaboration & Virgo Collaboration 2019p). Initially, two different Bayestar-based sky localizations were generated, one with the lower false alarm rate which included Livingston and Virgo data (sent 21 min after the trigger time) and one with contribution of the three instruments (sent 2 hr after the GW trigger time). A third skymap (LALInference) with all three interferometers was sent ~ 13.5 hr after the trigger time. The initial three interferometer 90% credible region was 38 deg^2 with a luminosity distance estimated at 276 ± 56 Mpc. The latest 90% credible region is 23 deg^2 with a luminosity distance of 267 ± 52 Mpc. With the small localization region, and its location in the Southern hemisphere,

the event was ideal for follow-up. However, no counterpart candidates remain after the extensive follow-up, with about 70 circulars produced (see GCN archive). As shown in Table 3, many survey systems covered a vast majority of the localization region, including ATLAS (Srivastav et al. 2019), DESGW-DECam (Soares-Santos et al. 2019), and TAROT (Klotz et al. 2019). We note here despite the small sky area and the intensive followed-up studies, we do not consider this object in the analysis due to its `HasRemnant` value.The joint coverage of MASTER and TAROT with 17 mag in clear filter within the first 3 hours was about 90% of the LALinference skymap.

2.5. *S190901ap*

LIGO/Virgo S190901ap was identified by L1 and V1 at 2019-09-01 23:31:01.838 UTC (LIGO Scientific Collaboration & Virgo Collaboration 2019t). The candidate is currently classified as BNS (86%) and terrestrial (14%). The latest 90% credible region is 14753 deg^2 with a luminosity distance of 241 ± 79 Mpc (LIGO Scientific Collaboration & Virgo Collaboration 2019u), whereas the initial 90% credible region was 13613 deg^2 with a luminosity distance of 242 ± 81 Mpc. Although considered as an interesting event due to a possible remnant, the large error box of thousands of square degrees led to a bit less interest in following-up the event (see $\approx$ 44 reports in GCN archive). However, survey instruments such as GOTO (Ackley et al. 2019b), ZTF (Kool et al. 2019) and MASTER (Lipunov et al. 2019e) observed more than 30% of the localiztion; in particular, ZTF covered more than 70%.

2.6. *S190910d*

LIGO/Virgo S190910d was identified as a compact binary merger candidate by H1 and L1 at 2019-09-10 01:26:19.243 UTC (LIGO Scientific Collaboration & Virgo Collaboration 2019v). The candidate is currently classified as NSBH (98%) and terrestrial (2%). With an initial 90% credible region of 3829 deg^2 with a luminosity distance of 606 ± 197 Mpc, the latest 90% credible region is 2482 deg^2 with a luminosity distance of 632 ± 186 Mpc (LIGO Scientific Collaboration & Virgo Collaboration 2019x). Relatively few instruments participated in the follow-up of this object (see ≈ 25 reports in GCN archive). However, network instruments such as ZTF (Anand et al. 2019), GRANDMA-TAROT (Noysena et al. 2019), and MASTER (Lipunov et al. 2019f) observed 25% of the skymap or more.

2.7. *S190910h*

LIGO/Virgo S190910h was identified as a compact binary merger candidate by only one detector (L1) at 2019-09-10 08:29:58.544 UTC (LIGO Scientific Collaboration & Virgo Collaboration 2019w). The candidate is currently classified as BNS (61%) and terrestrial (39%). The initial 90% credible region was 24226 deg^2 with a luminosity distance of 241 ± 89 Mpc. The latest 90% credible region is 24264 deg^2 with a luminosity distance of 230 ± 88 Mpc (LIGO Scientific Collaboration & Virgo Collaboration 2019y). Even fewer instruments participated in the follow-up of this object (see $\approx$ 20 reports in GCN archive) due to the previous alert (S190910d) which was just a few hours before, in addition to the very large localization. Only ZTF covered a significant portion of the localization (about 34% in g/r-band, Stein et al. 2019a).

2.8. *S190923y*

The candidate S190923y was identified by H1 and L1 at 2019-09-23 12:55:59.646 UTC. So far, only low-latency classification and sky localizations are publicly available (LIGO Scientific Collaboration & Virgo Collaboration 2019z). S190923y is classified with NSBH (>68%) and Terrestrial (32%) with low latency estimation. The bayestar initial sky localization area gives a 90 % credible region of 2107 deg^2 with a luminosity distance of 438 ± 133 Mpc. Due to the large uncertainty of the sky localization area and the distance luminosity above the completeness of most of the galaxy catalogs (see $\approx$ 17 reports in GCN archive), S190923y has been followed-up by surveys as GRANDMA-TAROT and MASTER in optical bands at $\approx$ 18 mag (Turpin et al. 2019; Lipunov et al. 2019h).

2.9. *S190930t*

The candidate was identified by L1 at 2019-09-30 14:34:07.685 UTC. So far, only low-latency classification and sky localizations are publicly available (LIGO-Virgo collaboration 2019). S190930t is classified with NSBH (74%) and Terrestrial (26%). The bayestar initial sky localization area gives a 90% credible region of 24220 deg^2 with a luminosity distance of 108 ± 38 Mpc. A number of the survey instruments, including ATLAS (Smartt et al. 2019b), MASTER (Lipunov et al. 2019g), and ZTF Stein et al. (2019b) covered a significant portion of the localization above $\approx$ 19.5 mag.

2.10. *Summary*

There are a few takeaways from the above. The first is that dedicated robotic facilities, either in their generic survey mode or performing target of opportunity observations, are present throughout all events. Facilities such as TAROT, ZTF, and MASTER, all robotic survey instruments, contributed to kilonova searches for the

vast majority of objects. However, we conducted calculation of joint coverage of the sky localization area for two different alerts S190510g and S190814bv with the three networks. The improvement in terms of time spent for exploring a large portion of the skymap is not huge due to the missing coordination of the individual groups. However, this approach might help in terms of having a certain location on the sky re-observed several times which potentially improves the constraints or detection prospects upon further data analysis. As can be seen from the table, other robotic survey systems also imaged portions of the localizations (for example, with their routine searches for near earth objects), but these serendipitous observations and associated new candidates were not always reported publicly. This may motivate use of the central reporting databases, if only to assess the level of coverage. In addition, one notices that, generally, the participation from other systems, at the candidate identification level at least, seemed to have dropped off as the semester went along.

3. MODELING KILONOVA AND DERIVING POSSIBLE LIMITS FROM OBSERVATIONS

3.1. *Kilonova modelling*

We will employ three different kilonova models based on Kasen et al. (2017), Bulla (2019), and Hotokezaka & Nakar (2019) deriving constraints on possible kilonova lightcurves and their connected ejecta properties. With the use of multiple models, we hope to reduce systematic effects. For Model I and Model II, we employ a Gaussian Process Regression based interpolation (Doctor et al. 2017) to create a surrogate model for arbitrary ejecta properties (see Coughlin et al. (2018a,b) for further details). The idea of this algorithm is to create interpolated, surrogate models for bolometric lightcurves, photometric lightcurves, or spectral energy distribution in sparse simulation sets typically provided by modeling software. For the photometric lightcurves, in particular, each passband is individually interpolated onto the same time array of 0.1 days and analyzed separately. To support the interpolation, we perform a singular value decomposition (SVD) of a matrix composed of these lightcurves (separately for each passband); using this, we find eigenvalues and eigenvectors, which we will interpolate across the parameter space. To do so, we use the `sci-kit learn` (Pedregosa et al. 2011) implementation of Gaussian process regression (GPR, Rasmussen & Williams 2006), which is a statistical interpolation method which produces a posterior distribution on a function f given known values of f at a few points in the parameter space. Model III is semi-analytic.

Model I, [Kasen et al., 2017]: For the models presented in Kasen et al. (2017), each lightcurve depends on the ejecta mass $M_{\rm ej}$, the mass fraction of lanthanides $X_{\rm lan}$, and the ejecta velocity $v_{\rm ej}$. To simplify the analysis, we use a 1-component model which captures the broad features of AT2017gfo as shown in Coughlin et al. (2017), in contrast to the use of a 2-component model (Coughlin et al. 2018b) which improves the fit slightly but doubles the number of free parameters. We compute lightcurves consistent with the following prior choices: $-3 \leq \log_{10}(M_{\rm ej}/M_\odot) \leq 0$, $0 \leq v_{\rm ej} \leq 0.3\,c$. For the ejecta velocity, this covers the range used in the Kasen et al. (2017) simulation set; for the ejecta masses, where the simulation set covers $-3 \leq \log_{10}(M_{\rm ej}/M_\odot) \leq -1$, taking the prior to an ejecta mass of $1 M_\odot$ was chosen for the purpose of upper limits that did not depend on the upper bound. For the lanthanide fraction, we will pin the values to $X_{\rm lan} = [\,10^{-9}, 10^{-5}, 10^{-4}, 10^{-3}, 10^{-2}, 10^{-1}]$; note that for ATF2017gfo, assuming the exact same model, a lanthanide fraction of $10^{-3.54}$ described the observational data best Coughlin et al. (2018b).

Model II, [Bulla, 2019]: For the 2-component models presented in Bulla (2019), each lightcurve depends on four parameters: the ejecta mass $M_{\rm ej}$, the temperature at 1 day after the merger T_0, the half-opening angle of the lanthanide-rich component Φ (with $\Phi = 0$ and $\Phi = 90°$ corresponding to one-component lanthanide-free and lanthanide-rich models, respectively) and the observer viewing angle $\theta_{\rm obs}$ (with $\cos\theta_{\rm obs} = 0$ and $\cos\theta_{\rm obs} = 1$ corresponding to a system viewed edge-on and face-on, respectively). Unlike Kasen et al. (2017), models by Bulla (2019) do not solve the full radiative transfer equation but rather simulate radiation transport for a given multi-dimensional ejecta morphology adopting parametrized opacities as input. The main advantage over Model I is the possibility to compute viewing-angle dependent observables for self-consistent multi-dimensional geometries in place of combining one-component models with different compositions and thus neglecting the interplay between different components. For this article, we compute lightcurves consistent with $-3 \leq \log_{10}(M_{\rm ej}/M_\odot) \leq 0$, $15° \leq \Phi \leq 30°$ and $0 \leq \cos\theta_{\rm obs} \leq 1$, while the temperature is fixed to the following values: $T_0 = [3000, 5000, 7000, 9000]$ K. Note that for ATF2017gfo, $T_0 = 5000$ K, $\Phi = 30°$, and $\cos\theta_{\rm obs} = 0.9$ described the observational data best (Dhawan et al. 2019). Similar to the Kasen et al. (2017) model, the simulation set covers $-3 \leq \log_{10}(M_{\rm ej}/M_\odot) \leq -1$, and we extend the prior to an ejecta mass of $1 M_\odot$.

Model III, [Hotokezaka and Nakar 2019]: For the 2-component models presented in Hotokezaka & Nakar (2019), the light curves are computed based on the Arnett analytic model (Arnett 1982) and a black body spectrum with a specific temperature at the photosphere. It assumes spherical ejecta of which the inner part is composed of high-opacity material and the outer part is composed of low-opacity material. In this model, thermalization of gamma-rays and electrons produced by each radioactive decay is taken into account according to their injection energy. Each light curve depends on $M_{\rm ej}$, the ejecta velocity $v_{\rm ej}$, the dividing velocity between the inner and outer part and the opacity of the 2-components, $\kappa_{\rm low}$ and $\kappa_{\rm high}$. The same prior range for the ejecta mass and velocity as in Model I is used. The model also depends on the lower and upper limit of the velocity distribution, which we set as free parameters within the range of $v_{\rm min}/v_{\rm ej} \in [0.1, 1.0]$ and $v_{\rm max}/v_{\rm ej} \in [1.0, 2.0]$.

Model-independent remarks: Model I, Model II, and Model III use similar nuclear heating rates $\epsilon_{\rm nuc}$, in units of ergs per second per gram. Model I assumes $\epsilon_{\rm nuc} = 10^{10}\, t^{-1.3}$ erg g^{-1} s^{-1} where t is in days (Metzger et al. 2010). Model II, instead, adopts heating rates from Korobkin et al. (2012), $\epsilon_{\rm nuc} = \epsilon_0 \left(\frac{1}{2} - \frac{1}{\pi}\arctan\frac{t-t_0}{\sigma}\right)^{\alpha} \left(\frac{\epsilon_{\rm th}}{0.5}\right)$, with $\epsilon_0 = 2 \times 10^{18}$ erg g^{-1} s^{-1}, $t_0 = 1.3$ s, $\sigma = 0.11$ s, $\alpha = 1.3$ and $\epsilon_{\rm th} = 0.5$. In principle, Model III computes the radioactive power using the solar r-process abundance pattern with a minimum atomic mass number of 85. This is however computationally too expensive when sampling over many light curves, so in the analysis presented in Section 3.2 we fix the heating rate to the same as Model II. Although the previous formula provides a better description of nuclear heating rates at short timescales, $t \lesssim 10$ s, the agreement between the different rates is excellent at epochs of interest in this study, $t \gtrsim 1$ d.

Within our analysis, we compare the lightcurves to one-sided Gaussian distributions, where we have taken the mean to be the upper limit from the telescope in the given passband and the mean distance from the gravitational-wave skymaps. We include a distance variation in our analysis by sampling over a changing "zeropoint" in the lightcurves consistent with the distance uncertainty stated in the GW alerts. This is computed by adding a distance modulus consistent with the distance variation from the localizations. While this approach does not account for the exact three-dimensional skymap, it provides representative constraints and limits.

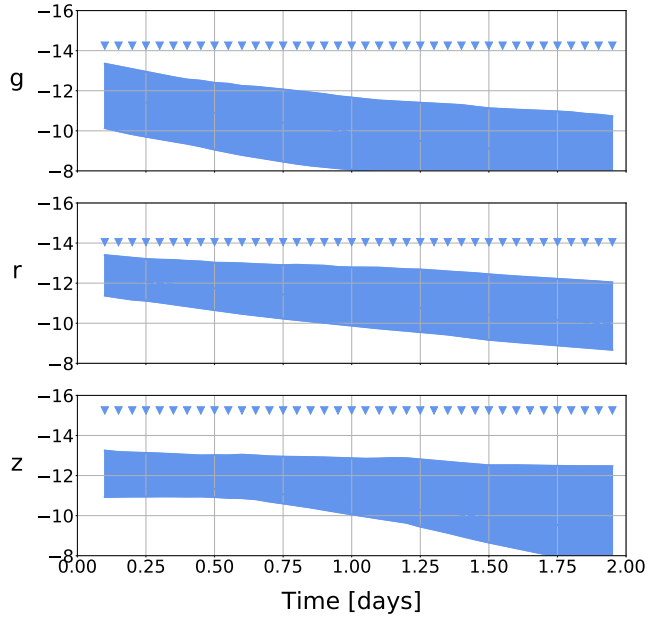

Figure 1. Variety of lightcurves consistent with the Dark Energy Camera based g/r/z limits on S190510g (Andreoni et al. 2019b), where we show median and 90% contours for lightcurves based on the Kasen et al. (2017) model.

Figure 1 gives an example of this approach for the candidate S190510g using the model of Kasen et al. (2017). It shows the upper limits derived from the Dark Energy Camera in horizontal lines for the three photometric bands g, r, and z. The absolute magnitudes correspond to the mean of the gravitational-wave distance. We also plot an example lightcurve consistent with these constraints. These include the uncertainty in distance sampling. Histograms of the ejecta masses (and other quantities) are made based on these lightcurves, creating the distributions derived in the following analyses.

3.2. *Ejecta mass limits*

In this section, we provide ejecta mass constraints from comparing different lightcurve models to observational upper limits for S190425z, S190426c, S190510g, S190901ap and S190910h. Specifically, we compute ejecta mass constraints for different values of one key quantity for each model: the lanthanide fraction (Model I), the temperature (Model II) and the opacities (Model III). Constraints on the ejecta mass are controlled by the impact of these three different parameters on the predicted kilonova brightness and color. Increasing the lanthanide fraction ($X_{\rm lan}$, Model I) and opacities ($\kappa_{\rm low}$ and $\kappa_{\rm high}$, Model III) shifts the escaping radiation to longer wavelengths and, thus, leads to the transition

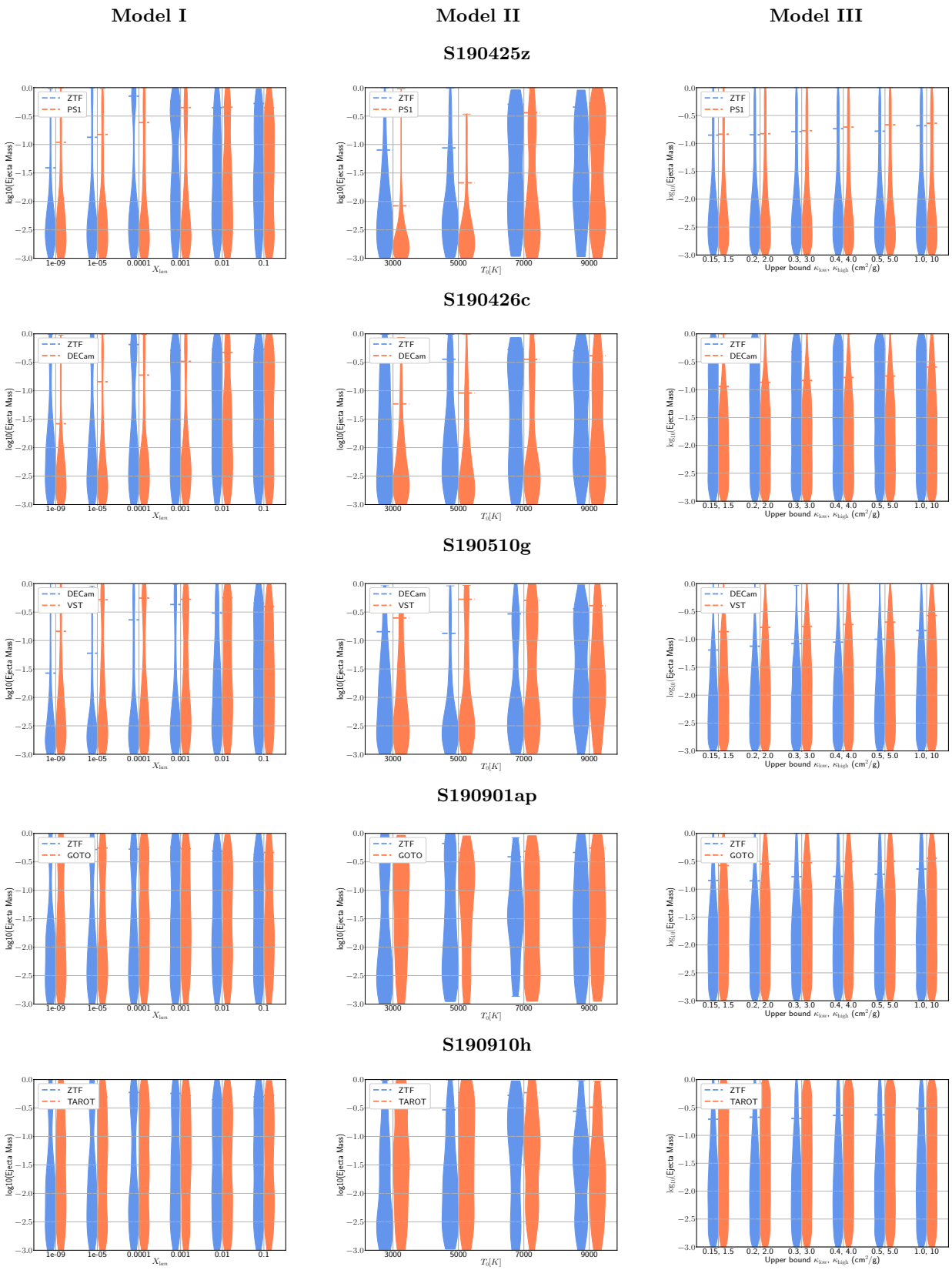

Figure 2. Probability density for the total ejecta mass for all considered events and all employed lightcurve models. From the top down, the events are S190425z, S190426c, S190510g, S190901ap, and S190910h. From the left to the right, we show constraints as a function of lanthanide fraction for based on the Kasen et al. (2017) model, as a function of temperature for the Bulla (2019) model with $\Phi = 0°$, and as a function of the opacity of the 2-components, $\kappa_{\rm low}$ and $\kappa_{\rm high}$. For S190425z, we use the ZTF (left, Kasliwal et al. (2019a)) and PS1 (right, Smith et al. (2019)) limits. For S190426c, we use the ZTF (Kasliwal et al. 2019b) and the DECam (Goldstein et al. 2019b) limits. For S190510g, we use DECam (Andreoni et al. 2019b) and VST (Grado et al. 2019a). For, S190901ap, we use the ZTF (Kool et al. 2019) and GOTO (Ackley et al. 2019b) observations. For S190910h, we use the ZTF (Stein et al. 2019a) and TAROT (Barynova et al. 2019b) observations.

from a "blue" to a "red" kilonova. The impact of the temperature (Model II) on the brightness and color depends on the epoch since merger. However, at phases when data are most constraining ($\lesssim 2$ d) an increase in temperature results in a shift of the emitted radiation from redder to bluer wavelengths. In particular, moving temperature from 3000 to 9000 K produces increasingly fainter kilonovae in both optical and near-infrared bands at these epochs.

Because of the different color predictions, telescopes observing in different regions of the spectrum are associated with different ejecta mass limits. For instance, optical telescopes are generally more constraining to "blue" kilonovae that have low lanthanide fractions.

S190425z: The top row of figure 2 shows the ejecta mass constraints for S190425z based on observations from ZTF (left, Kasliwal et al. (2019a)) and PS1 (right, Smith et al. (2019)). We mark the 90% confidence with a horizontal dashed line. In general, the constraints on ejecta mass for the low lanthanide fractions are stronger than available for the "red kilonovae," which are hidden in the redder photometric bands, cf. Model I. This is a result of using optical telescopes, which cover a large percentage of the sky localization, but are generally more constraining to "blue" kilonovae, i.e. those that have low lanthanide fractions. The i-band observations of PS1 lead to stronger constraints on the red side than is possible with ZTF for Model II, with similar constraints for Model I and Model III. With the higher intrinsic luminosities from Model II, the constraints in the redder bands from PS1 lead to notable improvements in the constraints. These constraints are not realized in Model I and Model III due to their lower intrinsic luminosities. We find that the different treatments of the heating rates and radiative transport, yield significantly different ejecta mass constraints than imposed by the effective opacity, temperature, and lanthanide fraction differences, i.e., differences between the three models are larger than within the individual models. Most notably, Model II produces, across all considered temperature ranges, the most stringent constraints. Consequently, while Model I and Model III only disfavor (in the most optimistic scenarios) ejecta masses $M_{\rm ej} \lesssim 0.1 M_\odot$, which is very hard to achieve for a BNS merger, Model II places upper bounds on the ejecta mass of $M_{\rm ej} \lesssim 0.03 M_\odot$ for temperatures at or below $5000K$.

S190426c: The second row of figure 2 shows the ejecta mass constraints for S190426c based on the observations from ZTF (Kasliwal et al. 2019b) and the DECam (Goldstein et al. 2019b). Despite the smaller sky area requiring coverage and therefore generally deeper exposures, the larger distance to this object leads to limits that are worse than for the first event. However, for a number of parameter combinations, we find that ejecta masses above $\sim 0.1 M_\odot$ are ruled out based on the DECam observations. Furthermore, as for S190425z, one obtains tighter constraints for blue kilonova (low lanthanide fractions and opacities) for Model I and Model III, and for redder kilonovae in Model II.

S190510g: The third row of figure 2 shows the ejecta mass constraints for S190510g based on observations from DECam (Andreoni et al. 2019b) and VST (Grado et al. 2019a). The relative improvement of sensitivity between ZTF and DECam offsets the relative difference in distance estimates, yielding very similar ejecta mass constraints between the two binary neutron star coalescence candidates, i.e., S190510g and S190425z. The inclusion of the three bands, g-, r-, and z-band observations with DECam produces measurable constraints in both the blue and red bands; for example, with Model I, $M_{\rm ej}$ is $\lesssim 0.025 M_\odot$ for the lowest lanthanide fractions.

S190901ap: The fourth row of figure 2 shows the ejecta mass constraints for S190901ap based on observations from ZTF (Kool et al. 2019) and GOTO (Ackley et al. 2019b). Due to the large sky localization covering more than 10,000 deg^2, there was relatively minimal EM follow-up investigation. The larger distance to this potential BHNS system results in the shallowest constraints on ejecta mass for all considered candidates.

S190910h: The final row of figure 2 shows the ejecta mass constraints for S190910h based on observations from ZTF (Stein et al. 2019a) and TAROT (Barynova et al. 2019b). Due to the large sky localization covering more than 20,000 deg^2, there was relatively minimal EM follow-up investigation, and therefore, similar to the event above, there were essentially no constraints.

Summary: Considering the five individual constraints, we find that S190425z and S190426c provide overall the tightest constraints for a BNS and BHNS candidate, respectively. However, our analysis shows that even for these events, no constraints can be obtained with Model III or for Model I in case for ejecta with high lanthanide fractions. These loose constraints are mainly caused by the large distance to the individual candidate events, which are generally several times further away than GW170817. Considering the results obtained from Model II, we will describe in the next section how potential ejecta mass constraints lead to constraints on the binary properties of BNS and BHNS candidates. However, we want to emphasize that there are large systematic differences between the lightcurve models and that the entire sky area provided by LIGO and Virgo has not been covered for all triggers. Thus,

the following analysis should be rather interpreted as a proof of principle.

4. CONSTRAINING THE BINARY PARAMETERS

Within this section, we present as a proof of principle possible constraints for the binary properties of the BNS candidate S190425z and the BHNS candidate S190426c (under the assumption that the source location was covered within the EM follow-up campaign). We focus on the results of Model II with a fixed temperature of 5000K[4]. This leads to a maximum total ejecta masses of $0.03M_\odot$ for S190425z and $0.09M_\odot$ for S190426c.

4.1. *The binary neutron star candidate S190425z*

To ensure that the ejected material is massive enough to trigger a bright EM counterpart, the final remnant should not collapse promptly to a black hole (BH) after the merger. As mentioned in the introduction, prompt collapse formation depends dominantly on the total mass of the binary. As shown in Bauswein et al. (2013) the total mass of the binary M has to be below a characteristic threshold mass:

$$M_{\rm thr} = \left(2.380 - 3.606\frac{M_{\rm TOV}}{R_{1.6M_\odot}}\right) M_{\rm TOV} \qquad (1)$$

with $M_{\rm TOV}$ being the maximum supported mass for a spherical NS and $R_{1.6M_\odot}$ the radius of a $1.6M_\odot$ NS. Recently, the threshold mass estimate was updated by Köppel et al. (2019) incorporating a non-linear dependence on the maximum allowed compactness and Agathos et al. (2019) derived a prompt-collapse threshold estimate based on new numerical relativity simulations, mainly publicly available at `http://www.computational-relativity.org` (Dietrich et al. 2018). For our rough estimates presented here, we will use, for simplicity, the criterion given in Bauswein et al. (2013).

While for close GW events it would be a valid assumption that all configurations without an EM counterpart have masses above the prompt threshold mass, $M > M_{\rm thr}$, this assumption does not hold for systems with distances much larger than the one for GW170817, e.g., for S190425z. In general, the total ejecta mass, for which our previous analysis provided some upper limits, is related to the debris disk mass formed after the merger; here, we use the disk mass estimate presented in Coughlin et al. (2018a), where $M_{\rm disk}$ was a function on $M/M_{\rm thr}$:

$$\log_{10}\left(m_{\rm disk}\left[M_{\rm tot}/M_{\rm thr}\right]\right) = \max\left(-3,\ a\left(1 + b\tanh\left[\frac{c - M_{\rm tot}/M_{\rm thr}}{d}\right]\right)\right) \qquad (2)$$

with the fitting parameters a, b, c, d; see Coughlin et al. (2018a). We emphasize that this estimate was based on a suite of numerical relativity simulations for equal-mass or near equal-mass systems, high mass ratio systems might lead to more massive disks Kiuchi et al. (2019) The mass of the disk wind is then $M_{\rm wind} = fM_{\rm disk}$ with the unknown conversion factor f. This efficiency parameter remains very uncertain (Fernández et al. 2015; Siegel & Metzger 2018; Fernández et al. 2019; Christie et al. 2019) and we will vary it for our BNS analysis, $f \in [0.1, 0.4]$.[5] Since a fraction of the ejecta will also be released dynamically during the merger, not all of the total ejecta comes from disk winds. As an indication, we present the disk wind estimate in figure 3 assuming 100% of the total ejecta mass for S190425z are connected to the wind ejecta (solid black line), 75% of the total mass is assigned to winds (dashed line), and half of the total ejecta comes from disk wind ejecta (dotted line).

The two panels in figure 3 refer to different choices of the maximum TOV-mass $2.07M_\odot$ for the top and $2.30M_\odot$ for the bottom panel. These values are motivated by the recent observation of J0740+6620 (Cromartie et al. 2019) and the upper bound on the maximum mass following from GW170817, e.g. (Margalit & Metzger 2017; Rezzolla et al. 2018; Shibata et al. 2019). In addition, we assume a radius $R_{1.6M_\odot}$ of 11.1km in the top and 13.9km in the bottom panel, as derived in Coughlin et al. (2018a).These combinations of $M_{\rm TOV}$ and $R_{1.6M_\odot}$ include the most extreme scenarios in terms of stiff and soft EOSs, and, thus, provide boundaries for our analysis. Considering the scenario for a very soft EOS, we find that the total mass of S190425z lies presumably above $2.40M_\odot$ if the efficiency factor if about 20%. Contrary for an efficiency factor of 20% and a very stiff EOS, the total mass of S190425z would presumably be $2.9M\odot$.

[4] With the chosen temperature of 5000K the predictions of Model II agree best with AT2017gfo (Dhawan et al. 2019). Thus, this temperature choice seems best suited for our analysis.

[5] Existing 3D simulations, which seed the accretion disk with a purely toroidal or purely poloidal magenetic field, fall at the high end of that interval, $f \sim [0.3 - 0.4]$. We conservatively allow for lower values of f to account for the possibility that about half of that ejecta is produced at early times, in magnetically-driven winds that appear to depend on the strength and stucture of the magnetic field and may still disappear for the small-scale turbulent magnetic fields that are most likely created in a neutron star merger.

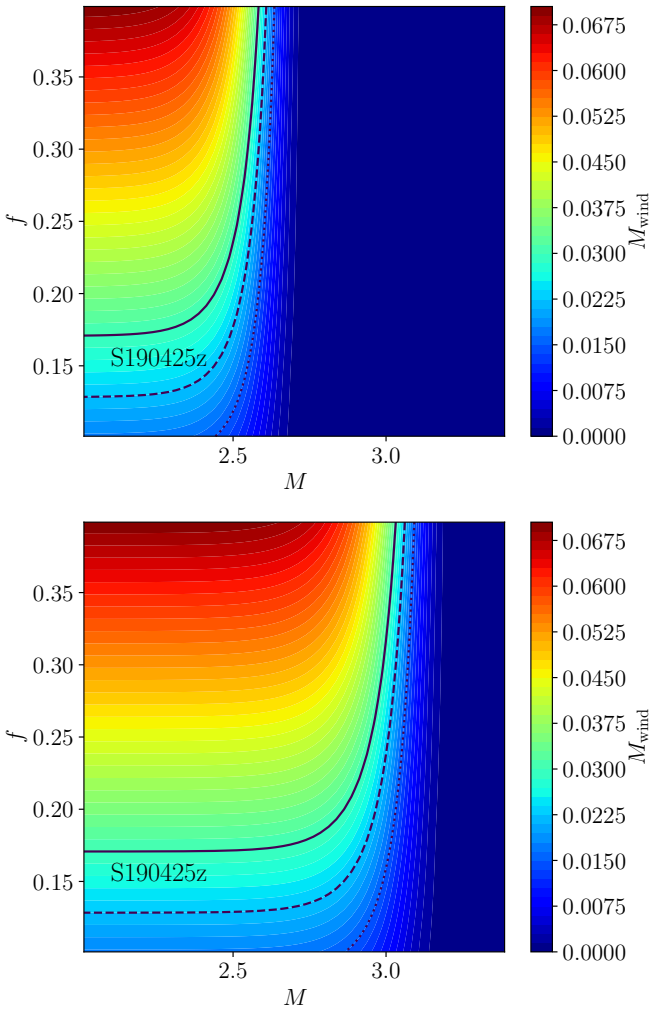

Figure 3. Disk wind ejecta as a function of the conversion factor f and the total mass of the binary M. We include the upper bounds from S190425z using Model II for 5000K assuming that the disk wind accounts for the entire ejecta mass (solid line), 75% (dashed line) or for 50% of the total ejecta (dotted line). The top panel assumes an EOS with a maximum TOV mass of $2.07M_\odot$ and a radius of $R_{1.6M_\odot} = 11.1$km, while the bottom panel uses $M_{\rm TOV} = 2.30M_\odot$ and $R_{1.6M_\odot} = 13.9$km.

4.2. *The black hole - neutron star candidate S190426c*

Similarly for BHNS systems, the absence of an observed kilonova constrains the initial parameters of the binary. As for the BNS case, the outflows from BHNS mergers can be divided into the dynamical ejecta, which is produced at the time of merger and typically lanthanide-rich (Deaton et al. 2013; Foucart et al. 2014; Kyutoku et al. 2018), and magnetically-driven or neutrino-driven disk winds produced in the $1-10$ seconds following the merger, which have a more uncertain composition (Fernández et al. 2015; Just et al. 2015; Siegel & Metzger 2018; Fernández et al. 2019). The dynamical ejecta for neutron stars within the range of parameters used in numerical simulations so far is well modeled by the fit of Kawaguchi et al. (2016). Extrapolating that fit to more compact stars, however, leads to unphysical results (i.e. an increase in the ejected mass for more compact stars). Here, we use the modified formula

$$\frac{M_{\rm dyn}}{M_{\rm NS}^b} = \max\left(0, a_1 Q^{n_1}(1-2C_{\rm NS}) - a_2 Q^{n_2}\frac{c^2 R_{\rm ISCO}}{GM_{\rm BH}} + a_3\right) \quad (3)$$

with $Q = M_{\rm BH}/M_{\rm NS}$, $M_{\rm NS}^b$ the baryon mass of the neutron star, $C_{\rm NS} = GM_{\rm NS}/(R_{\rm NS}c^2)$ its compactness, $R_{\rm ISCO}$ the radius of the innermost stable circular orbit around the black hole, and $a_1 = 0.007116, a_2 = 0.001436, a_3 = -0.0276, n_1 = 0.8636, n_2 = 1.6840$ (see Krüger et al., in prep, for a more detailed discussion). Note that $R_{\rm ISCO}$ is computed for circular orbits around a black hole of dimensionless spin $\chi_{\rm eff} = \chi_\parallel$, with $\chi_\parallel$ the component of the black hole spin aligned with the orbital angular momentum of the binary. As a result, the ejected mass has a strong dependence in the aligned component of the black hole spin. The total mass in the bound accretion disk surrounding the remnant black hole can be estimated by subtracting $M_{\rm dyn}$ from the total amount of mass remaining outside of the black hole after merger $M_{\rm out}$. We compute $M_{\rm out}$ following the fit to numerical results provided in Foucart et al. (2018). Similarly to $M_{\rm dyn}$, $M_{\rm out}$ depends on the mass ratio of the system, the compactness of the neutron star, and the aligned component of the black hole spin. The mass in the disk winds is then $M_{\rm wind} = f(M_{\rm out} - M_{\rm dyn})$. Since the BHNS case contains already a larger number of free parameters, we fix the conversion factor to $f \gtrsim 0.15$ (Fernández et al. 2015; Siegel & Metzger 2018; Fernández et al. 2019; Christie et al. 2019).

If S190426c was a BHNS merger within the region of the sky observed by ZTF and DECAM, and we assume the constraints obtained with Model II at 5000K, we argued that $M_{\rm ej} = M_{\rm dyn} + M_{\rm wind}$ has to be less than $0.09M_\odot$. Practically, this can be converted into a constrain excluding part of the 3-dimensional parameter space of $(Q, C_{\rm NS}, \chi_\parallel)$. Figure 4 visualizes this constraint as a maximum allowed value for the component of the dimensionless black hole spin *aligned with the orbital angular momentum* of the binary, as a function of neutron star size and binary mass ratio. We see that with this upper bound, the constraints on the parameter space of BHNS binaries are fairly weak: only large aligned black hole spins combined with low-mass stars and relatively stiff equations of state can possibly be ruled out.

5. SUMMARY

We have presented an overview of the extensive searches for EM transients associated with a number of GW event triggers within the first half of the third

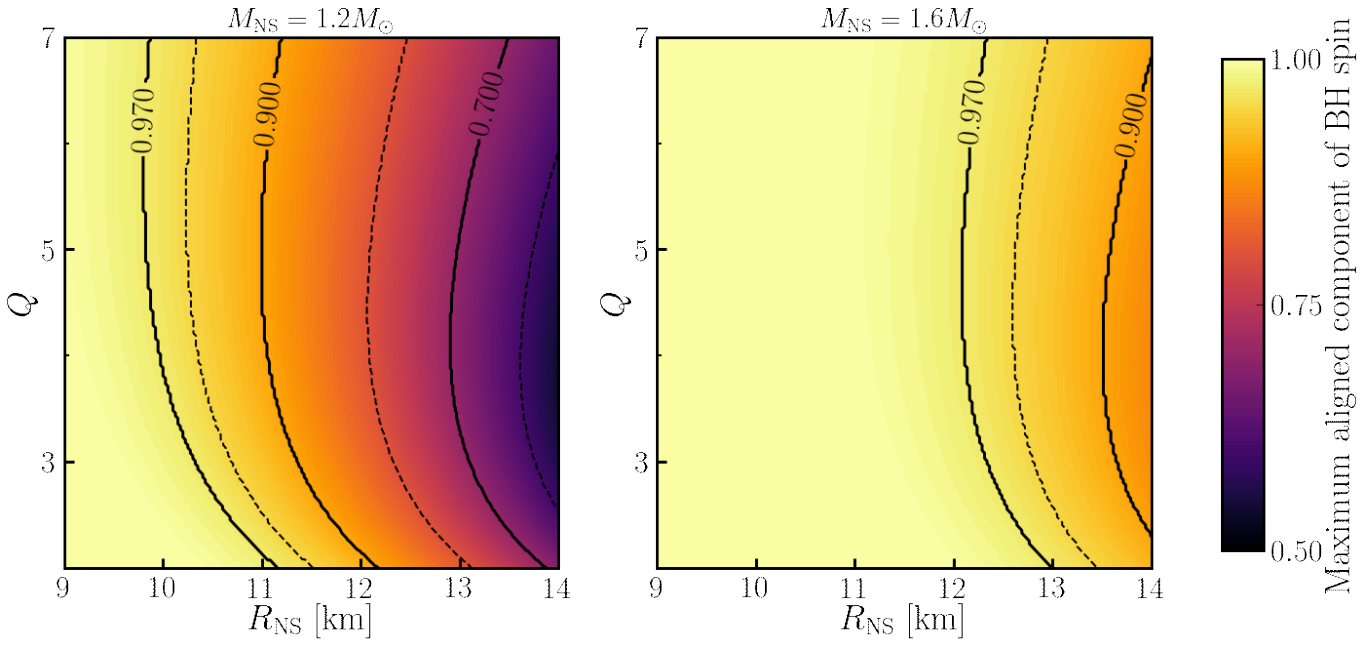

Figure 4. Maximum aligned component of the black hole spin as a function of neutron star radius and binary mass ratio for S190426c, if that event was a BHNS merger *within* the region covered by follow-up observations. We show results for $M_{\rm NS} = 1.2M_\odot$ (left) and $M_{\rm NS} = 1.6M_\odot$, and require $M_{\rm ej} < 0.09M_\odot$ (Model II for 5000K). Dashes lines correspond to maximum spins of $0.6, 0.8, 0.95$, and solid lines to maximum spins of $0.7, 0.9, 0.97$. Only a small part of the parameter space (large aligned spin, low mass neutron stars) can possibly be ruled out be observations. The constraints for more massive stars ($M_{\rm NS} = 1.6M_\odot$) are not reliable since the analytical models have not been tested for spins greater than ~ 0.9.

observing run of Advanced LIGO and Advanced Virgo. Assuming that the individual sources were located in the covered sky region of the follow-up observations, we use three different kilonova models to derive possible upper limits on the ejecta mass compatible with the non-observation of EM signals for S190425z, S190426c, S190510g, S190901ap, and S190910h. Possibly informative constraints are obtained for S190425z and S190426c with the model of Bulla (2019). However, systematic uncertainties between different kilonova models are large and currently the dominating source of error in our analysis.

Based on our results, we computed potential lower limits on the total mass of S190425z from the non-existence of EM counterparts and find that it should have a total mass above $2.5M_\odot$ if we assume a soft and $2.9M_\odot$ if we assume a stiff EOS. Similarly, assuming that S190426c originated from a BHNS merger, we find that the non-observation of a kilonova could rule out large aligned black hole spins combined with low-mass stars (for stiff EOSs).

Our simple analysis shows that even without direct GW information, beyond the provided skymap and classification probability, source properties can be constrained[6]. More importantly, inverting our approach, one sees that a fast estimation of the total mass can potentially be used to classify if potential GW candidates will cause bright EM counterparts. A similar approach has been recently outlined in Margalit & Metzger (2019).

In general, the limits derived on the ejecta mass for the events in the first six months of O3 are not striking, which shows that one should be striving to take deeper observations, perhaps at the cost of a smaller sky coverage. Assuming that AT2017gfo is representative, "interesting" limits are $\sim 0.05\,M_\odot$, giving a ballpark limit to strive for. Those observations are most important at low latency, i.e., at times when kilonovae are brightest. In addition to adding and/or employing guiding to take longer observations, it might motivate the creation and use of stacking pipelines for survey facilities, for which this may be atypical.

Michael Coughlin is supported by the David and Ellen Lee Postdoctoral Fellowship at the California Institute of Technology. Tim Dietrich acknowledges support by the European Union's Horizon 2020 research and in-

[6] While we used `HasRemnant` to downselect the events, we did not rely on its results for the analysis.

novation program under grant agreement No 749145, BNSmergers. Sarah Antier is supported by the CNES Postdoctoral Fellowship at Laboratoire Astroparticle et Cosmologie. MB acknowledges support from the G.R.E.A.T research environment funded by the Swedish National Science Foundation. Francois Foucart gratefully acknowledges support from NASA through grant 80NSSC18K0565 and from the NSF through grant PHY-1806278. The lightcurve fitting / upperlimits code used here is available at: https://github.com/mcoughlin/gwemlightcurves.

REFERENCES

Abbott B. P. e. a., 2017, Phys. Rev. Lett., 119, 161101

Abbott B.P. e. a., 2019,] 10.3847/1538-4357/ab0e8f, 875, 161

Abbott et al. 2017a, Nature, 551, 85

Abbott B. P., et al., 2017b, Astrophys. J., 848, L12

Abbott B. P., et al., 2017c, The Astrophysical Journal Letters, 848, L13

Ackley K., et al., 2019a, GRB Coordinates Network, 25337

Ackley K., et al., 2019b, GRB Coordinates Network, 25654

Agathos M., Zappa F., Bernuzzi S., Perego A., Breschi M., Radice D., 2019

Anand S., et al., 2019, GRB Coordinates Network, 25706

Andreoni I., et al., 2019a

Andreoni I., et al., 2019b, Astrophys. J., 881, L16

Arcavi et al. 2017, Nature, 551, 64 EP

Arnett W. D., 1982, ApJ, 253, 785

Baker T., Bellini E., Ferreira P. G., Lagos M., Noller J., Sawicki I., 2017, Phys. Rev. Lett., 119, 251301

Barynova K., et al., 2019a, GRB Coordinates Network, 25666

Barynova K., et al., 2019b, GRB Coordinates Network, 25780

Bauswein A., Baumgarte T. W., Janka H. T., 2013, Phys. Rev. Lett., 111, 131101

Bauswein A., et al., 2017, The Astrophysical Journal Letters, 850, L34

Bellm E. C., et al., 2018, Publications of the Astronomical Society of the Pacific, 131, 018002

Bhalerao V., et al., 2019, GRB Coordinates Network, 24258

Blazek M., et al., 2019a, GRB Coordinates Network, 24227

Blazek M., et al., 2019b, GRB Coordinates Network, 24327

Bulla M., 2019, MNRAS, 489, 5037

Capano C. D., et al., 2019

Christensen N., et al., 2019, GRB Coordinates Network, 25599

Christie I. M., Lalakos A., Tchekhovskoy A., Fernández R., Foucart F., Quataert E., Kasen D., 2019

Cook D. O., et al., 2019, GRB Coordinates Network, 24232

Coughlin M., Dietrich T., Kawaguchi K., Smartt S., Stubbs C., Ujevic M., 2017, ApJ, 849, 12

Coughlin M. W., Dietrich T., Margalit B., Metzger B. D., 2018a, arXiv e-prints,

Coughlin M. W., et al., 2018b, Monthly Notices of the Royal Astronomical Society, 480, 3871

Coughlin M. W., Dietrich T., Heinzel J., Khetan N., Antier S., Christensen N., Coulter D. A., Foley R. J., 2019a

Coughlin M. W., et al., 2019b, arXiv e-prints, p. arXiv:1907.12645

Coulter D. A., et al., 2017, Science, 358, 1556

Creminelli P., Vernizzi F., 2017, Phys. Rev. Lett., 119, 251302

Cromartie H. T., et al., 2019

Dado S., Dar A., 2019

De K., et al., 2019, GRB Coordinates Network, 24187

Deaton M. B., et al., 2013, Astrophys. J., 776, 47

Dekany Smith et al., 2019, Submitted to PASP

Dhawan S., Bulla M., Goobar A., Sagués Carracedo A., Setzer C. N., 2019, arXiv e-prints, p. arXiv:1909.13810

Dichiara S., et al., 2019, GRB Coordinates Network, 25352

Dietrich T., Ujevic M., 2017, Class. Quant. Grav., 34, 105014

Dietrich T., et al., 2018, Class. Quant. Grav., 35, 24LT01

Doctor Z., Farr B., Holz D. E., Pürrer M., 2017, preprint, (arXiv:1706.05408)

Eichler D., Livio M., Piran T., Schramm D. N., 1989, Nature, 340, 126

Etienne Z. B., Liu Y. T., Shapiro S. L., Baumgarte T. W., 2009, Phys. Rev., D79, 044024

Ezquiaga J. M., Zumalacrregui M., 2017, Phys. Rev. Lett., 119, 251304

Fernández R., Kasen D., Metzger B. D., Quataert E., 2015, Mon. Not. Roy. Astron. Soc., 446, 750

Fernández R., Tchekhovskoy A., Quataert E., Foucart F., Kasen D., 2019, Mon. Not. Roy. Astron. Soc., 482, 3373

Foucart F., 2012, Phys. Rev., D86, 124007

Foucart F., et al., 2014, Phys. Rev., D90, 024026

Foucart F., Hinderer T., Nissanke S., 2018, Phys. Rev., D98, 081501

Goldstein D. A., et al., 2019a, Astrophys. J., 881, L7

Goldstein D. A., et al., 2019b, GRB Coordinates Network, 24257

Grado A., et al., 2019a, GRB Coordinates Network, 24484
Grado A., et al., 2019b, GRB Coordinates Network, 25371
Graham M. J., et al., 2019, Publications of the Astronomical Society of the Pacific, 131, 078001
Groot P., et al., 2019, GRB Coordinates Network, 25340
Hankins M., et al., 2019a, GRB Coordinates Network, 24284
Hankins M., et al., 2019b, GRB Coordinates Network, 25358
Hotokezaka K., Nakar E., 2019
Hotokezaka K., Kiuchi K., Kyutoku K., Okawa H., Sekiguchi Y.-i., Shibata M., Taniguchi K., 2013, Phys. Rev., D87, 024001
Hotokezaka K., Nakar E., Gottlieb O., Nissanke S., Masuda K., Hallinan G., Mooley K. P., Deller A., 2019, Nature Astron.
Im M., et al., 2019, GRB Coordinates Network, 24466
Just O., Bauswein A., Pulpillo R. A., Goriely S., Janka H. T., 2015, Mon. Not. Roy. Astron. Soc., 448, 541
Kapadia S. J., et al., 2019
Kasen D., Metzger B., Barnes J., Quataert E., Ramirez-Ruiz E., 2017, Nature, 551, 80 EP
Kasliwal M. M., et al., 2019a, GRB Coordinates Network, 24191
Kasliwal M. M., et al., 2019b, GRB Coordinates Network, 24283
Kawaguchi K., Kyutoku K., Shibata M., Tanaka M., 2016, Astrophys. J., 825, 52
Kilpatrick C., et al., 2019, GRB Coordinates Network, 25350
Kim J., et al., 2019, GRB Coordinates Network, 25342
Kiuchi K., Kyutoku K., Shibata M., Taniguchi K., 2019, Astrophys. J., 876, L31
Klotz A., et al., 2019, GRB Coordinates Network, 25338
Kool E., et al., 2019, GRB Coordinates Network, 25616
Köppel S., Bovard L., Rezzolla L., 2019, Astrophys. J., 872, L16
Korobkin O., Rosswog S., Arcones A., Winteler C., 2012, Monthly Notices of the Royal Astronomical Society, 426, 1940
Kyutoku K., Ioka K., Okawa H., Shibata M., Taniguchi K., 2015, Phys. Rev., D92, 044028
Kyutoku K., Kiuchi K., Sekiguchi Y., Shibata M., Taniguchi K., 2018, Phys. Rev., D97, 023009
LIGO Scientific Collaboration Virgo Collaboration 2019a, GRB Coordinates Network, 24168
LIGO Scientific Collaboration Virgo Collaboration 2019b, GRB Coordinates Network, 24228
LIGO Scientific Collaboration Virgo Collaboration 2019c, GRB Coordinates Network, 24237
LIGO Scientific Collaboration Virgo Collaboration 2019d, GRB Coordinates Network, 24279
LIGO Scientific Collaboration Virgo Collaboration 2019e, GRB Coordinates Network, 24411
LIGO Scientific Collaboration Virgo Collaboration 2019f, GRB Coordinates Network, 24442
LIGO Scientific Collaboration Virgo Collaboration 2019g, GRB Coordinates Network, 24448
LIGO Scientific Collaboration Virgo Collaboration 2019h, GRB Coordinates Network, 24489
LIGO Scientific Collaboration Virgo Collaboration 2019i, GRB Coordinates Network, 24591
LIGO Scientific Collaboration Virgo Collaboration 2019j, GRB Coordinates Network, 24656
LIGO Scientific Collaboration Virgo Collaboration 2019k, GRB Coordinates Network, 25087
LIGO Scientific Collaboration Virgo Collaboration 2019l, GRB Coordinates Network, 25187
LIGO Scientific Collaboration Virgo Collaboration 2019m, GRB Coordinates Network, 25208
LIGO Scientific Collaboration Virgo Collaboration 2019n, GRB Coordinates Network, 25296
LIGO Scientific Collaboration Virgo Collaboration 2019o, GRB Coordinates Network, 25324
LIGO Scientific Collaboration Virgo Collaboration 2019p, GRB Coordinates Network, 25333
LIGO Scientific Collaboration Virgo Collaboration 2019q, GRB Coordinates Network, 25367
LIGO Scientific Collaboration Virgo Collaboration 2019r, GRB Coordinates Network, 25442
LIGO Scientific Collaboration Virgo Collaboration 2019s, GRB Coordinates Network, 25549
LIGO Scientific Collaboration Virgo Collaboration 2019t, GRB Coordinates Network, 25606
LIGO Scientific Collaboration Virgo Collaboration 2019u, GRB Coordinates Network, 25614
LIGO Scientific Collaboration Virgo Collaboration 2019v, GRB Coordinates Network, 25695
LIGO Scientific Collaboration Virgo Collaboration 2019w, GRB Coordinates Network, 25707
LIGO Scientific Collaboration Virgo Collaboration 2019x, GRB Coordinates Network, 25723
LIGO Scientific Collaboration Virgo Collaboration 2019y, GRB Coordinates Network, 25778
LIGO Scientific Collaboration Virgo Collaboration 2019z, GRB Coordinates Network, 25814
LIGO-Virgo collaboration 2019, GRB Coordinates Network, 25876
Lattimer J. M., Schramm D. N., 1974, ApJL, 192, L145
Lattimer J. M., Schramm D. N., 1976, ApJ, 210, 549

Lee W. H., Ramirez-Ruiz E., 2007, New Journal of Physics, 9, 17
Li L.-X., Paczynski B., 1998, The Astrophysical Journal Letters, 507, L59
Li B., et al., 2019, GRB Coordinates Network, 24465
Lipunov V., et al., 2017, The Astrophysical Journal Letters, 850, L1
Lipunov V., et al., 2019a, GRB Coordinates Network, 24167
Lipunov V., et al., 2019b, GRB Coordinates Network, 24236
Lipunov V., et al., 2019c, GRB Coordinates Network, 24436
Lipunov V., et al., 2019d, GRB Coordinates Network, 25322
Lipunov V., et al., 2019e, GRB Coordinates Network, 25609
Lipunov V., et al., 2019f, GRB Coordinates Network, 25694
Lipunov V., et al., 2019g, GRB Coordinates Network, 25712
Lipunov V., et al., 2019h, GRB Coordinates Network, 25812
Lundquist M. J., et al., 2019, arXiv e-prints, p. arXiv:1906.06345
Margalit B., Metzger B. D., 2017, Astrophys. J., 850, L19
Margalit B., Metzger B. D., 2019
Masci F. J., et al., 2018, Publications of the Astronomical Society of the Pacific, 131, 018003
McBrien O., et al., 2019, GRB Coordinates Network, 24197
Melandri A., et al., 2019, GRB Coordinates Network, 24340
Metzger B. D., et al., 2010, Monthly Notices of the Royal Astronomical Society, 406, 2650
Mochkovitch R., Hernanz M., Isern J., Martin X., 1993, Nature, 361, 236
Mooley K. P., et al., 2017, Nature, 554, 207 EP
Nakar E., 2007, Phys. Rept., 442, 166
Narayan R., Paczynski B., Piran T., 1992, ApJL, 395, L83
Niino Y., et al., 2019, GRB Coordinates Network, 24299
Noysena K., et al., 2019, GRB Coordinates Network, 25749
Paczynski B., 1991, AcA, 41, 257
Pannarale F., Tonita A., Rezzolla L., 2011, Astrophys. J., 727, 95
Pedregosa F., et al., 2011, Journal of Machine Learning Research, 12, 2825
Pereyra E., et al., 2019, GRB Coordinates Network, 25737
Radice D., Dai L., 2019, Eur. Phys. J., A55, 50
Radice D., Perego A., Zappa F., Bernuzzi S., 2018, The Astrophysical Journal Letters, 852, L29
Rasmussen C. E., Williams C. K. I., 2006, Gaussian Processes for Machine Learning. MIT Press
Rezzolla L., Most E. R., Weih L. R., 2018, Astrophys. J., 852, L25
Roberts L. F., Kasen D., Lee W. H., Ramirez-Ruiz E., 2011, The Astrophysical Journal Letters, 736, L21
Sakstein J., Jain B., 2017, Phys. Rev. Lett., 119, 251303
Sari R., Piran T., Narayan R., 1998, ApJL, 497, L17
Savchenko V., et al., 2017, The Astrophysical Journal, 848, L15
Shappee B., et al., 2019, GRB Coordinates Network, 24309
Shibata M., Zhou E., Kiuchi K., Fujibayashi S., 2019
Siegel D. M., Metzger B. D., 2018, Astrophys. J., 858, 52
Singer et al. 2019, GRB Coordinates Network, 25343
Smartt S., et al., 2019a, GRB Coordinates Network, 24517
Smartt S., et al., 2019b, GRB Coordinates Network, 25922
Smith K. W., et al., 2019, GRB Coordinates Network, 24210
Soares-Santos et al. 2017, The Astrophysical Journal Letters, 848, L16
Soares-Santos M., et al., 2019, GRB Coordinates Network, 25336
Srivastav S., et al., 2019, GRB Coordinates Network, 25375
Steeghs D., et al., 2019a, GRB Coordinates Network, 24224
Steeghs D., et al., 2019b, GRB Coordinates Network, 24291
Stein R., et al., 2019a, GRB Coordinates Network, 25722
Stein R., et al., 2019b, GRB Coordinates Network, 25899
Tanvir N. R., Levan A. J., Fruchter A. S., Hjorth J., Hounsell R. A., Wiersema K., Tunnicliffe R. L., 2013, Nature, 500, 547 EP
Troja E., et al., 2017, Nature, 551, 71 EP
Turpin D., et al., 2019, GRB Coordinates Network, 25847
Valenti et al. 2017, The Astrophysical Journal Letters, 848, L24
Veitch J., et al., 2015, Phys. Rev. D, 91, 042003
Watson A. M., et al., 2019, GRB Coordinates Network, 24310
Wei J., et al., 2019, GRB Coordinates Network, 25648
Xu D., et al., 2019a, GRB Coordinates Network, 24190
Xu D., et al., 2019b, GRB Coordinates Network, 24285
Xu D., et al., 2019c, GRB Coordinates Network, 24286
Xu D., et al., 2019d, GRB Coordinates Network, 24476
Yoshida M., et al., 2019, GRB Coordinates Network, 24450
Zhu Z., et al., 2019, GRB Coordinates Network, 24475

APPENDIX

Table 2. Reports of the observations by various teams of the sky localization area of gravitational-wave alerts of the possible BNS candidates S190425z, S190510g, S190901ap, S190910h and S190930t. Teams that employed "galaxy targeting" during their follow-up are not mentioned here. In the case where numbers were not reported or provided upon request, we recomputed some of them; if this was not possible, we add −.

Telescope	Filter	Limit mag	Delay aft. GW (h)	Duration (h)	GW sky localization area name	coverage (%)	reference
S190425z							
ATLAS	o-band	19.5	0.8	6.2	bayestar ini	37	McBrien et al. (2019)
CNEOST	clear	≈ 20	27.5	4.8	bayestar ini	10	Xu et al. (2019b)
GOTO	L-band	20.5	11.7	8.9	bayestar ini	30	Steeghs et al. (2019a)
GRANDMA-TAROT	clear	17.5	6.7	< 63	LALInference	3	Blazek et al. (2019a)
GROWTH-Gattini-IR	J-band	15.5	1.0	27.8	LALInference	19	De et al. (2019)
MASTER-network	clear	≈ 18.5	≈ 0.0	144	bayestar ini	37	Lipunov et al. (2019a)
Pan-STARRS	i-band	21.5	1.3	< 19	bayestar ini	28	Smith et al. (2019)
SAGUARO	g-band	≈ 21	1.3	1.3	bayestar ini	3	Lundquist et al. (2019)
Xinglong-Schmidt	clear	18	4.5	0.9	bayestar ini	3	Xu et al. (2019a)
Zwicky Transient Facility	g/r-band	≈ 21	1.0	27.8	LALInference	21	Kasliwal et al. (2019a)
S190510g							
ATLAS	o-band	19.5	4.2	< 12	LALinference	4	Smartt et al. (2019a)
CNEOST	clear	≈ 18.5	9.9	3.3	bayestar ini	13	Li et al. (2019)
Dabancheng/HMT	clear	≈ 18	13.0	6.0	bayestar ini	≈ 8	Xu et al. (2019d)
GRAWITA-VST	r-sloan	22	21.1	< 6	LALInference	50	Grado et al. (2019a)
GROWTH-DECAM	g/r/z-band	21.7/22.3/21.2	3.0	18.5	LALInference	65	Andreoni et al. (2019b)
HSC	Y-band	22.7	< 6	< 12	bayestar ini	12	Yoshida et al. (2019)
KMTNet	R-band	21.7	13.6	< 12	LALInference	66	Im et al. (2019)
MASTER-network	clear	≈ 18.5	≈ 0	144	bayestar ini	52	Lipunov et al. (2019c)
Pan-STARRS	w/i-band	20.5	4.2	< 12	LALInference	4	Smartt et al. (2019a)
Xinglong-Schmidt	clear	18.5	9.8	5.8	bayestar ini	19	Zhu et al. (2019)
DECAM-KMTNet	r-R band	> 22	3.0	< 24	LALInference	69	-
CNEOST-HMT-MASTER-Xinglong-TAROT	clear	> 18	1.0	< 24	LALInference	71	-
S190901ap							
GOTO	L-band	20	0.1	54	bayestar ini	28	Ackley et al. (2019b)
GRANDMA-TAROT	clear	17.5	0.4	< 58.6	LALInference	9	Barynova et al. (2019a)
MASTER-network	clear	≈ 18.5	5.5	168	bayestar ini	32	Lipunov et al. (2019e)
SVOM-GWAC	R-band	16.3	12.0	9	bayestar ini	16	Wei et al. (2019)
Zwicky Transient Facility	g/r-band	20.7/20.7	3.6	∼ 72	LALInference	73	Kool et al. (2019)
S190910h							
GRANDMA-TAROT	clear	18	10.5	< 129	LALInference	1	Barynova et al. (2019b)
MASTER-network	clear	≈ 18.5	2.6	144	bayestar ini	8	Lipunov et al. (2019g)
Zwicky Transient Facility	g/r-band	20.7/20.7	1.80	1.5	bayestar ini	34	Stein et al. (2019a)
S190930t							
ATLAS	o-band	19.5	0.0	144	bayestar ini	19	Smartt et al. (2019b)
MASTER-network	clear	≈ 18.5	≈ 0	72	bayestar ini	10	Lipunov et al. (2019g)
Zwicky Transient Facility	g/r-band	20.4/20.4	11.9	10.0	bayestar ini	45	Stein et al. (2019b)

Table 3. Reports of the observations by various teams of the sky localization area of gravitational-wave alerts of possible BHNS candidates S190426c, S190814bv, S190910d and S190923y. Teams that employed "galaxy targeting" during their follow-up are not mentioned here. In the case where numbers were not reported or provided upon request, we recomputed some of them; if this was not possible, we add −.

Telescope	Filter	Limit mag	Delay aft. GW (h)	Duration (h)	GW sky localization area name	coverage (%)	reference
S190426c							
ASAS-SN	g-band	≈ 18	-	≈ 24	bayestar ini	86	Shappee et al. (2019)
CNEOST	clear	≈ 20	1.3	3.5	bayestar ini	35	Xu et al. (2019c)
DDOTI/OAN	w-band	≈ 18.5	14.7	4.9	bayestar ini	≈ 37	Watson et al. (2019)
GOTO	g-band	19.9	5.3	8.9	LALInference	54	Steeghs et al. (2019b)
GRANDMA-OAJ	r-band	19.6	6.3	4.9	bayestar ini	11	Blazek et al. (2019b)
GRAWITA-Asiago	r-band	≈ 16	6.9	0.5	LALInference	2	Melandri et al. (2019)
GROWTH-DECAM	r/z-band	22.9/22.5	7.6	11.5	LALInference	8.0	Goldstein et al. (2019a)
GROWTH-Gattini-IR	J-band	≈ 14.5	11.8	9.8	bayestar ini	92	Hankins et al. (2019a)
GROWTH-INDIA	r-band	20.5	2.0	29.4	bayestar ini	4	Bhalerao et al. (2019)
J-GEM	clear	20	19	-	bayestar ini	-	Niino et al. (2019)
MASTER-network	clear	≈ 18.5	≈ 0	144	bayestar ini	53	Lipunov et al. (2019b)
SAGUARO	g-band	≈ 21	41.8	≈ 24	bayestar ini	5	Lundquist et al. (2019)
Zwicky Transient Facility	g/r-band	≈ 21	13.0	31.3	bayestar ini	75	Kasliwal et al. (2019b)
S190814bv							
ATLAS	o-band	> 16	< 12	24.0	LALInference	99	Srivastav et al. (2019)
DESGW-DECam	r/i-band	23.4, 22.6	9.5	≈ 96	LALInference	90	Soares-Santos et al. (2019)
DDOTI/OAN	w-band	≈ 18.5	10.8	3.9	LALInference	90	Dichiara et al. (2019)
GOTO	L-band	18.4	3.5	5.0	LALInference	83	Ackley et al. (2019a)
GRAWITA-VST	r-sloan	≈ 22	11.7	1.3	LALInference	65	Grado et al. (2019b)
GROWTH-Gattini-IR	J-band	≈ 17.0	8.9	96.0	bayestar ini	90	Hankins et al. (2019b)
KMTNet	R-band	22.0	8.4	< 12	LALInference	98	Kim et al. (2019)
MASTER-network	clear	≈ 18	0.4	6.7	bayestar ini	98	Lipunov et al. (2019d)
MeerLICHT	u/q/i-band	18.5/19.7/19.1	2.0	5.1	bayestar HLV	95	Groot et al. (2019)
Pan-STARRS	i/z-band	20.8/20.3	15.5	2.55	LALInference	89	Smartt et al. (2019a)
Swope	r-band	≈ 20.0	6.3	5.1	LALinference	42	Kilpatrick et al. (2019)
GRANDMA-TCA	clear	18.0	3.0	2.5	bayestar HLV	27	Klotz et al. (2019)
GRANDMA-TRE	clear	17.0	0.5	1.0	LALinference	76	Christensen et al. (2019)
Zwicky Transient Facility	g/r/i-band	20.3	13.3	1.7	bayestar ini HLV	86	Singer et al. (2019)
MASTER-TAROT	clear	> 17	0.5	< 3	LALInference	89	-
S190910d							
DDOTI/OAN	w-band	≈ 18.5	3.0	4.7	LALInference	5	Pereyra et al. (2019)
GRANDMA-TAROT	clear	≈ 17.5	1.0	< 67	LALInference	37	Noysena et al. (2019)
MASTER-network	clear	≈ 18.5	≈ 0	144	bayestar ini	25	Lipunov et al. (2019f)
Zwicky Transient Facility	g/r-band	20.8	1.5	1.5	bayestar ini	34	Anand et al. (2019)
S190923y							
GRANDMA-TAROT	clear	≈ 17.5	3.7	< 56.1	bayestar ini	26	Turpin et al. (2019)
MASTER-network	clear	≈ 18.5	≈ 0	144	bayestar ini	58	Lipunov et al. (2019h)